

# Statistical and systematic errors in cosmic microwave background maps

Hao Liu<sup>1,3</sup> and Ti-Pei Li<sup>1,2</sup>

## ABSTRACT

Sky temperature map of the cosmic microwave background (CMB) is one of the premier probes of cosmology. To minimize instrumentally induced systematic errors, CMB anisotropy experiments measure temperature differences across the sky using pairs of horn antennas with a fixed separation angle, temperature maps are recovered from temperature differences obtained in sky survey through a map-making procedure. The instrument noise, inhomogeneities of the sky coverage and sky temperature inevitably produce statistical and systematic errors in recovered temperature maps. We show in this paper that observation-dependent noise and systematic temperature distortion contained in released Wilkinson Microwave Anisotropy Probe (WMAP) CMB maps are remarkable. These errors can contribute to large-scale anomalies detected in WMAP maps and distort the angular power spectrum as well. It is needed to remake temperature maps from original WMAP differential data with modified map-making procedure to avoid observation-dependent noise and systematic distortion in recovered maps.

*Subject headings:* cosmic microwave background — cosmology: observations — methods: statistical

## 1. Map-making

The COBE and WMAP missions measure temperature differences between sky points using differential radiometers consisting of plus-horn and minus-horn (Smoot et al. 1990; Bennett et al. 2003a). Let denote  $t_i$  the temperature anisotropy at a sky pixel  $i$ . The raw

---

<sup>1</sup>Key Lab. of Particle Astrophys., Inst. of High Energy Phys., Chinese Academy of Sciences, Beijing

<sup>2</sup>Center for Astrophysics, Tsinghua University, Beijing, China; litp@ihep.ac.cn

<sup>3</sup>Graduate School of Chinese Academy of Sciences, Beijing

data in a certain band is a set of temperature differences  $\mathbf{d}$  between pixels in the sky. From  $N$  observations we have the following observation equations

$$\begin{aligned} t_{1+} - t_{1-} &= d_1 \\ t_{2+} - t_{2-} &= d_2 \\ \dots\dots\dots\dots\dots\dots \\ t_{N+} - t_{N-} &= d_N . \end{aligned} \tag{1}$$

The above equation system can be expressed by matrix notation

$$\mathbf{A}\mathbf{t} = \mathbf{d} . \tag{2}$$

Where the scan matrix of the experiment  $\mathbf{A} = (a(k, i))$ ,  $k = 1, \dots, N$  and  $i = 1, \dots, L$  with  $L$  being the total number of sky map pixels. The most of elements  $a(k, i) = 0$  except for  $a(k, i = k^+) = 1$  and  $a(k, i = k^-) = -1$ , where  $k^+$  denotes the pixel observed by the plus-horn and  $k^-$  the pixel observed by the minus-horn at an observation  $k$ .

The normal equation of Eq. 1 or Eq. 2 is

$$\mathbf{M}\mathbf{t} = \mathbf{A}^T\mathbf{d} \tag{3}$$

with  $\mathbf{M} = \mathbf{A}^T\mathbf{A}$ . The least-squares estimate of the sky map results from solving Eq. 3

$$\hat{\mathbf{t}} = \mathbf{M}^{-1}\mathbf{A}^T\mathbf{d} .$$

The WMAP team (Hinshaw et al. 2003) uses the following approximate formula to compute the iterative solution

$$\mathbf{t}^{(n+1)} = \tilde{\mathbf{M}}^{-1}(\mathbf{A}^T\mathbf{d} - \mathbf{A}^T\mathbf{A}\mathbf{t}^{(n)}) + \mathbf{t}^{(n)} , \tag{4}$$

where  $\tilde{\mathbf{M}}^{-1} = \text{diag}(\frac{1}{N_1}, \frac{1}{N_2}, \dots)$  is an approximate inverse of  $\mathbf{M}$  with  $N_i$  being the total number of observations for pixel  $i$ .

The use of approximate inverse matrix  $\mathbf{M}^{-1}$  is not necessary. Here we derive an iterative formula directly from the normal equation. The Eq. 3 can be expressed as

$$\begin{aligned} N_i^+ t_i - \sum_{k^+=i} t_{k^-} - \sum_{k^-=i} t_{k^+} + N_i^- t_i &= \sum_{k^+=i} d_k - \sum_{k^-=i} d_k , \\ &(i = 1, 2, \dots, L) . \end{aligned}$$

Where  $\sum_{k^+=i}$  means summing over  $N_i^+$  observations while the pixel  $i$  is observed by the plus-horn and  $\sum_{k^-=i}$  means summing over  $N_i^-$  observations while the pixel  $i$  is observed by

the minus-horn, and the total number of observations for the pixel  $i$  is  $N_i = N_i^+ + N_i^-$ . From the above equations we can derive the following iterative formula

$$t_i^{(n+1)} = \frac{1}{N_i} \left( \sum_{k^+=i} (d_k + t_{k^-}^{(n)}) - \sum_{k^-=i} (d_k - t_{k^+}^{(n)}) \right),$$

$$(i = 1, 2, \dots, L). \quad (5)$$

With Eq. 4 or Eq. 5 when the number  $n$  of iteration is large enough, we get the final solution  $\hat{t}_i = t_i^{(n)}$  for each pixel  $i$ . The Eq. 4 used by the WMAP team is an approximate formula and Eq. 5 is an exact one, but both has good performance for the differential data of a noiseless instrument. With Eq. 5 we can easily study the statistical and systematical errors induced by instrument noise, inhomogeneity of sky coverage, inhomogeneity of sky temperature, and unbalance between two sky side measurements.

## 2. Exposure-dependent noise

We can directly see from Eq. 5 that there exists exposure dependent noise in a recovered temperature map. The WMAP differencing assembly has instrument noise  $\mathbf{n}$  per observation, the real observation data  $d_k = t_{k^+} - t_{k^-} + n_k$ . The instrument noise is not negligible, e.g. the mean rms noise  $\sigma_0 = 6.7$  mK for the W4-band of WMAP (Limon et al. 2003). The obtained temperature differences  $d_k$  can be taken as a random variable with a standard error  $\sigma_0$ . The final iterative solution  $\hat{t}_i$  from Eq. 5 has a noise component being the mean of  $N_i$  variables, i.e. the temperature  $\hat{t}_i$  in a WMAP map for a sky pixel  $i$  has an exposure-dependent error

$$\sigma_i = \frac{1}{\sqrt{N_i}} \sigma_0. \quad (6)$$

By analyzing CMB maps from the first year WMAP (WMAP1) data, Tegmark et al. (2003) find both the CMB quadrupole and octopole having power along a particular spatial axis and more works (de Oliveira-Costa et al. 2004; Eriksen et al. 2004a; Schwarz et al. 2004; Jaffe et al. 2005) find that the axis of maximum asymmetry tends to lie close to the ecliptic axis. A similar anomaly was also found in COBE maps (Copi et al. 2006). The unexplained orientation of large-scale patterns of CMB maps in respect to the ecliptic frame is one of the biggest surprises in CMB studies (Starkman and Schwarz 2005). A notable asymmetry of temperature fluctuation power in two opposing hemispheres is also found in the WMAP1 and COBE results (Eriksen et al. 2004b; Hansen et al. 2004). After the release of WMAP results in 2006 March, similar large-scale anomalies are still detected in the WMAP3 data (Abramo et al. 2006; Jaffe et al. 2006; Copi et al. 2007; Land & Magueijo 2007; Eriksen et al. 2007;

Park et al. 2007; Vielva et al. 2007; Samal et al. 2008). The unexpected large-scale anomalies in CMB maps are extensively studied with different techniques, but their reasons still remain unclear. Here we show that the exposure-dependent noise should be an important source of detected anomalies.

## 2.1. Large-scale non-Gaussian modulation

Because the sky coverage of WMAP mission is inhomogeneous – the number of observations being greatest at the ecliptic poles and the ecliptic plane being most sparsely observed (Hinshaw et al. 2007), from Eq. 6 we know that the WMAP temperature maps contain inhomogeneous exposure-dependent noise components. The remarkable fact, the feature of large-scale anomalies detected in WMAP maps being very similar with the WMAP exposure pattern, strongly indicates the existence of such observational effect on WMAP maps. To address the large scale anomalies, such as asymmetry, alignment and low  $l$  power issues detected in WMAP data with different techniques, the WMAP team (Spergel et al. 2006) describe the observed temperature fluctuations,  $\hat{t}$ , as a Gaussian and isotropic random field,  $\mathbf{t}$ , modulated by a function  $f(\mathbf{n})$

$$\hat{t}(\mathbf{n}) = t(\mathbf{n})[1 + f(\mathbf{n})]$$

where  $f(\mathbf{n})$  is an arbitrary modulation function. They expand  $f(\mathbf{n})$  in spherical harmonics

$$f(\mathbf{n}) = \sum_{l=1}^{l_{max}} \sum_{l=-m}^m f_{lm} Y_{lm}(\mathbf{n})$$

and use maximum likelihood technique with a Markov Chain Monte Carlo solver to get the best fit values of  $f_{lm}$  with  $l_{max} = 2$  for the WMAP3 V-band map. The bottom panel of Fig. 1 is obtained based on the best fit coefficients, showing in a unifying manner the large scale anomalies in WMAP temperature fluctuations which is the same feature that has been identified in a number of papers on non-Gaussianity. We calculate the spherical harmonic coefficients  $f_{lm}$  with  $l_{max} = 2$  for the map of  $1/N$  with  $N$  being number of observations per sky pixel from the WMAP3 V-band data. The top panel of Fig. 1 shows the map of  $1/N$  reconstructed based on the coefficients  $f_{lm}$ . The middle panel shows the reconstructed result for the observation fluctuation map – the map of  $1/\sigma(N)$  where the rms variation  $\sigma(N) = \sqrt{\langle(N - \langle N \rangle)^2\rangle}$  calculated within a region of  $\sim 1^\circ$  side dimension for each sky pixel. The large-scale non-Gaussian modulation features of WMAP temperature map and scan pattern being similar for each other suggests that large scale anomalies detected in WMAP maps are most probably resulted from observation effect, not cosmological origin. In comparing

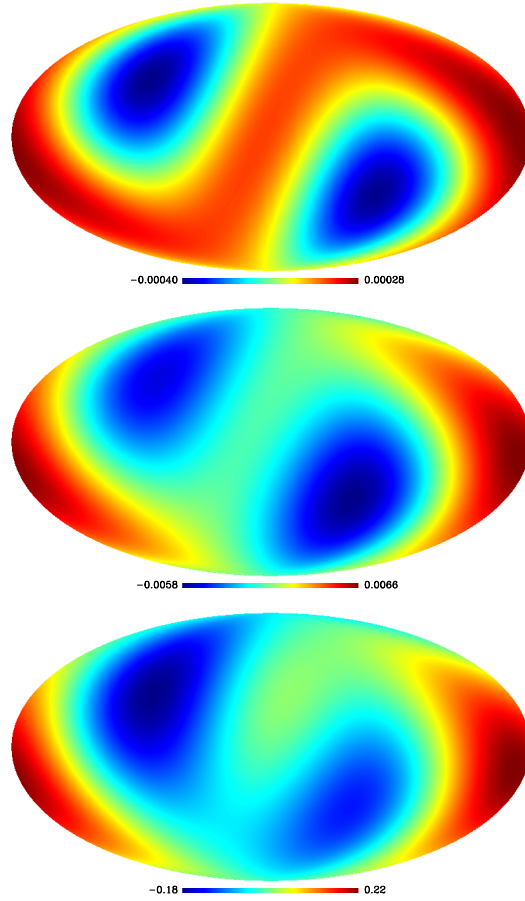


Fig. 1.— Large-scale non-Gaussian modulation features with  $l_{max} = 2$  for the WMAP3 V-band data . *Top panel:* large-scale feature of  $1/N$  map. *Middle panel:* large-scale feature of  $1/\sigma(N)$  map. *Bottom panel:* Best-fit large-scale modulation function  $f(\hat{\mathbf{n}})$  for temperature map.

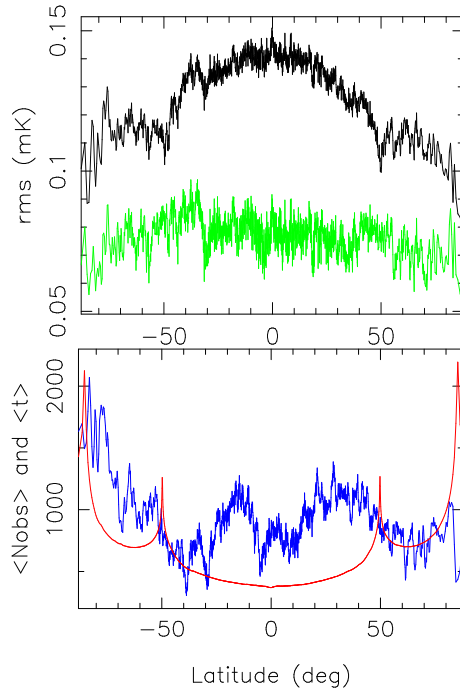


Fig. 2.— Latitude distributions from the WMAP3 foreground-cleaned Q1-band map in ecliptic coordinates. *Black line*: rms variation in the map,  $\sigma_0 = 2.27$  mK. *Green line*: residual rms after excluding the exposure-dependent anisotropy component by Eq. 7. *Red line*: average number of observations per sky pixel. *Blue line*: average map temperature (in mK, times by a factor of  $2.76 \times 10^4$ ).

the top and middle panels in Fig. 1, the modulation pattern for the observation fluctuation map is more similar to the detected anomalies shown in the bottom panel, indicating that the fluctuation of observation numbers could produce additional noise component to the recovered temperature map.

## 2.2. Alignment and planarity

To show the anisotropy noise, we compute the average rms variation  $\sqrt{\langle \hat{t}^2 \rangle}$  for the WMAP3 foreground-cleaned Q1-band temperature map at different latitudes; the results are shown by the black line in Fig. 2. The red line in Fig. 2 shows that of average number of observations per sky pixel. To modify the exposure-induced rms anisotropy, we use the following formula to get the residual variation

$$rms = \sqrt{\langle (\hat{t} - \langle \hat{t} \rangle)^2 \rangle - \langle \sigma_0^2 / N \rangle}. \quad (7)$$

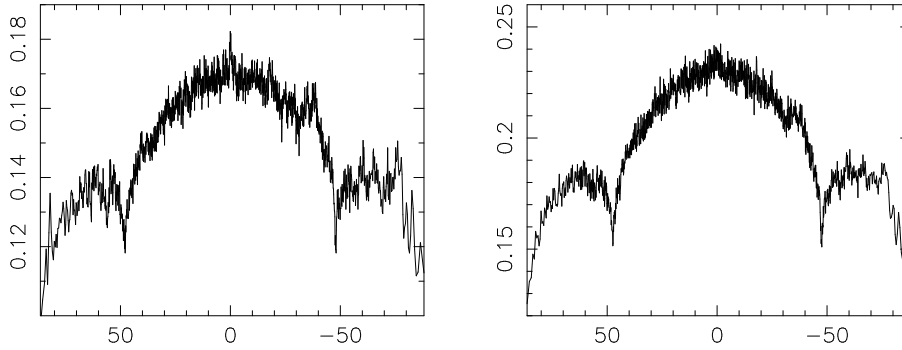


Fig. 3.— Latitude distributions of temperature rms variation from WMAP3 foreground-cleaned maps in ecliptic coordinates. *left*: V1 band,  $\sigma_0 = 3.29$  mK. *right*: W1 band,  $\sigma_0 = 5.83$  mK.

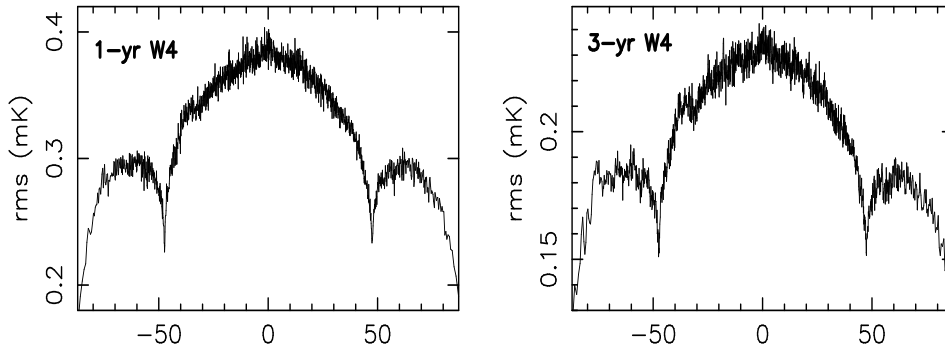


Fig. 4.— Latitude distributions of temperature rms variation from WMAP foreground-cleaned maps in ecliptic coordinates. *left*: WMAP1 W4 band,  $\sigma_0 = 6.7$  mK. *right*: WMAP3 W4 band,  $\sigma_0 = 6.7$  mK.

The residual rms of WMAP3 Q1-band, the green line in Fig. 2, shows that the latitude dependences are well excluded by using Eq. 7, or, in other words, the noise per pixel in the WMAP map is really exposure-dependent in a way described by Eq. 6.

Similar features are also found in other waveband maps and the combined frequency maps (TOH and ILC maps) as well. For example, Fig. 3 shows the results from WMAP3 V1 and W1 bands. The similarity of structures of latitude distribution of rms variation for different bands shown in Fig. 2 and Fig. 3 indicate that they are commonly originated from the ununiformity of sky exposure. The average pixel rms is 0.20 mK from  $N = 1.68 \times 10^6$  observations for W1 band, 0.15 mK from  $1.12 \times 10^6$  observations for V1 band and 0.13 mK from  $0.84 \times 10^6$  observations for Q1 band. The instrument noise  $\sigma_0$  for W1, V1 and Q1 band are 5.85, 3.29 and 2.27 mK respectively (Limon et al. 2003). We find that the ratios between

rms $\times\sqrt{N}$  of different bands are approximately equal to that between  $\sigma_0$  of corresponding bands, which is what expected by Eq. 6. Fig. 4 shows that the noise anisotropy for the three year WMAP W4-band map is almost the same as that for the first year map, not suppressed with data accumulation.

As demonstrated above, the released WMAP temperature maps contain considerable exposure-dependent noise. The remarkable similarity between the large scale non-Gaussian modulation feature of WMAP temperature fluctuation and exposure-pattern of WMAP observation, as shown in Fig. 1, suggests that large scale anomalies detected in WMAP maps are most probably resulted from observation effect, not astrophysical or cosmological origin.

For foreground removal the WMAP team produce the internal linear combination (ILC) map  $\mathbf{t}$  from the five frequency sky maps  $\mathbf{t}_i$  ( $i = 1, \dots, 5$ ) by  $\mathbf{t} = \sum_i w_i \mathbf{t}_i$  where the weights minimize the variance of final map,  $\text{Var}(\mathbf{t})$ , under the constraint  $\sum_i w_i = 1$ . For the region outside of the inner Galactic plane and by a nonlinear search, the weights  $w$  are found to be 0.109, -0.684, -0.096, 1.921, -0.250 for K, Ka, Q, V, and W bands, respectively (Bennett et al. 2003c). Eriksen et al. (2004b) make minimization of the variance under the constraint by means of Lagrange multipliers and obtain the solutions are the inverse covariance weights  $w_i = \frac{\sum_j C_{ij}^{-1}}{\sum_{j,l} C_{jl}^{-1}}$  with  $C_{ij}$  being the map-to-map covariance matrix.

It is needed to inspect the effect of exposure dependent noise in the ILC map, which is extensively used in cosmological analysis, although the WMAP team warns against its use for CMB studies because of the complex noise properties of this map (Limon et al. 2003). The left panel of Fig. 5 shows the latitude distribution of rms deviation from the WMAP3 ILC map. There exists a variation component monotonically decreasing from the southern pole to the northern pole, expressed roughly by the hand-drawn dotted line in the left panel of Fig. 5. The right panel shows the residual rms deviations after subtracting the north-south asymmetry component. From Fig. 5 we see that the procedure of linear combination with respect to the covariance between different frequencies can effectively depress the instrument noise. The latitude dependence of rms variation in the ILC map is weaker, but still visible with a structure similar to what observed in W, V and Q band. We can not make modification for the ILC map by sky exposure like what we do for Q, V and W data sets, because the ILC map is reconstructed by re-adding the data at different frequencies, it is difficult to assign an observation number  $N_i$  to a pixel  $i$ .

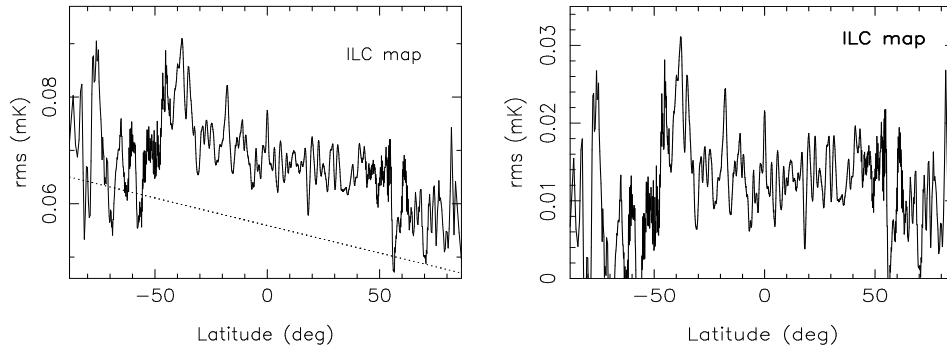


Fig. 5.— *Left*: RMS deviation of temperatures vs. ecliptic latitude for the three-year ILC map. The vertical coordinate is  $\sqrt{\langle \hat{t}^2 \rangle}$ , where  $\hat{t}$  denotes temperature anisotropies (in mK) at a certain latitude. *Right*: Residual rms deviations obtained from the curve shown in the left graph by subtracting the north-south asymmetry component (the dotted line in the left graph)

### 2.3. Pseudo sources

In studying the nature of discrete  $\gamma$ -ray sources discovered by the COS-B satellite experiment, we found that quite a lot apparent discrete sources revealed in the cross-correlation map with high significances (about half of sources in 2CG catalog) are pseudo-sources produced by the fluctuation of structured diffuse background of the galactic plane (Li & Wolfendale 1982). Here we use cross-correlation as another indicator to inspect the possible large-scale anomaly caused by the unevenly distributed noise in WMAP maps. We compute the cross-correlation function  $\mathbf{c}$  of the W4-band map  $\hat{t}$  and beam profile  $\mathbf{B}$  by  $\mathbf{c} = \mathbf{B}^T \hat{t}$ , and the standard deviation  $\sigma_c$  of the correlation map. The pixels with  $|c| \geq 3\sigma_c$  in ecliptic coordinates are shown in the left panel of Fig. 6. That the apparent features of point-like sources concentrated along the ecliptic plane are just generated by observation effect as this feature disappears after modifying WMAP temperatures by a factor of  $\frac{\sqrt{M_i}}{\sqrt{\langle M \rangle}}$  for both one-year and three-year data, as shown by the right column of Fig. 6. The result shown by Fig. 6 remind us that one should take a care before to claim a finding of CMB anomaly from observation maps before carefully considering the effect of exposure dependent noise.

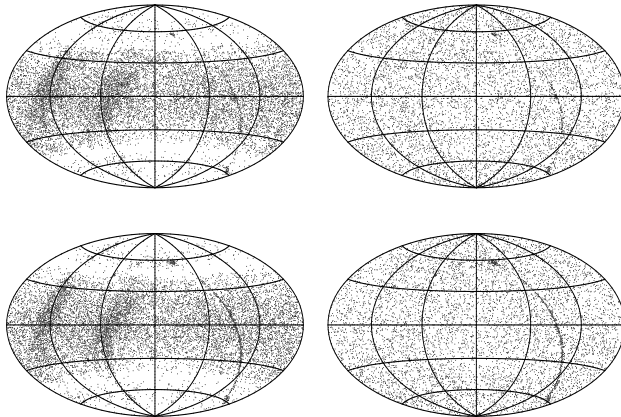


Fig. 6.— Cross-correlation map in ecliptic coordinates. Points show pixels with  $c \geq 3\sigma_c$ ,  $\mathbf{c}$  – cross-correlation of beam profile and sky temperature,  $\sigma_c$  – standard deviation of  $\mathbf{c}$ . *Left panel*, from W4-band map. *Right panel*, from modified W4-band map with multiplying temperatures by  $\frac{\sqrt{M_i}}{\sqrt{\langle M \rangle}}$ . *Top panel*, from WMAP1 data. *Bottom panel*, from WMAP3 data.

#### 2.4. North-south asymmetry

A remarkable character in Fig. 5 is the monotonically decline trend of rms variation from the south pole to the north pole in the ILC map. To show the north-south asymmetry quantitatively, we calculate the asymmetry ratio  $\text{rms}(\beta)/\text{rms}(-\beta)$  for different latitude  $\beta$ , where  $\text{rms}(\beta)$  is the average rms of sky pixels with latitude within  $\beta \pm 1.5^\circ$  in the northern hemisphere and  $\text{rms}(-\beta)$  is that in the south. The result is shown in Fig. 7. From Fig. 7 we see that there exists a systematic decrease of rms deviation from south to north with maximum asymmetry amplitude  $\sim 10\% - 20\%$ . For different ecliptic latitudes we calculate residual rms from the WMAP3 V-band foreground-cleaned map after modifying the exposure ununiformity by using Eq. 7, the result is shown in Fig. 8, where we also find a clear north-south asymmetry.

To see if the north-south asymmetry also exists in WMAP exposure, we calculate the exposure asymmetry ratio  $N(\beta)/N(-\beta)$  for W1, V1 and Q1 band separately, where  $N(\beta)$  is the three-year observation number contributing to the pixels with latitude within  $\beta \pm 1.5^\circ$  in the northern hemisphere and  $N(-\beta)$  is that in the south, the results are shown in Fig. 9. From Fig. 9 we see that there exists north-south asymmetry in WMAP sky survey: exposure increases from south to north with maximum amplitude  $\sim 2\% - 4\%$ . It is natural to explain the rms asymmetry by the exposure asymmetry as  $\sim 10\% - 20\%$  decreasing of rms deviation is just expected by  $\sim 2\% - 4\%$  increasing of exposure, provided that the linear combination can not suppress the common and systematic north-south asymmetry in multi frequencies

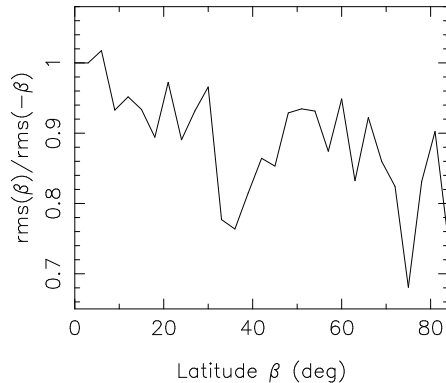


Fig. 7.— North-south asymmetry of rms deviation of temperatures in ILC map.  $\beta$  – ecliptic latitude.  $\text{rms}(\beta)/\text{rms}(-\beta)$  – ratio between rms deviations at the latitude  $\beta$  in the northern hemisphere and at that in the southern hemisphere.

and the exposure dependent noise follows Eq. 6,  $\text{rms} \propto 1/\sqrt{(N_i)}$ .

An apparent asymmetry in the distribution of fluctuation power in two opposing hemispheres with a remarkable absence of power in the vicinity of the northern ecliptic pole is observed from the WMAP1 Q, V, and W band sky maps (Eriksen et al. 2004b; Hansen et al. 2004). By analyzing the issue of power asymmetry with the WMAP3 ILC map and a model of an isotropic CMB sky modulated by a dipole field, Eriksen et al. (2007) find that the modulation amplitude is 11.4% and that the results on hemispherical power asymmetry are not sensitive to data set or sky cut. All of these features can be explained naturally by the effect of exposure dependent noise as we discuss above in this section.

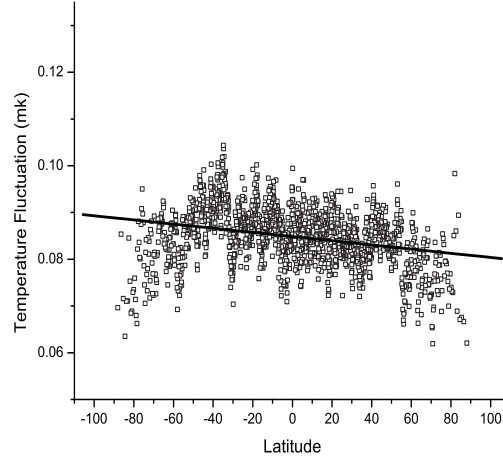


Fig. 8.— Ecliptic latitude dependence of residual temperature rms fluctuations of the foreground-cleaned WMAP3 V-band map. The rms fluctuations are modified by using Eq. 7. The best-fit line  $y = -4.46 \times 10^{-5}x + 0.085$ .

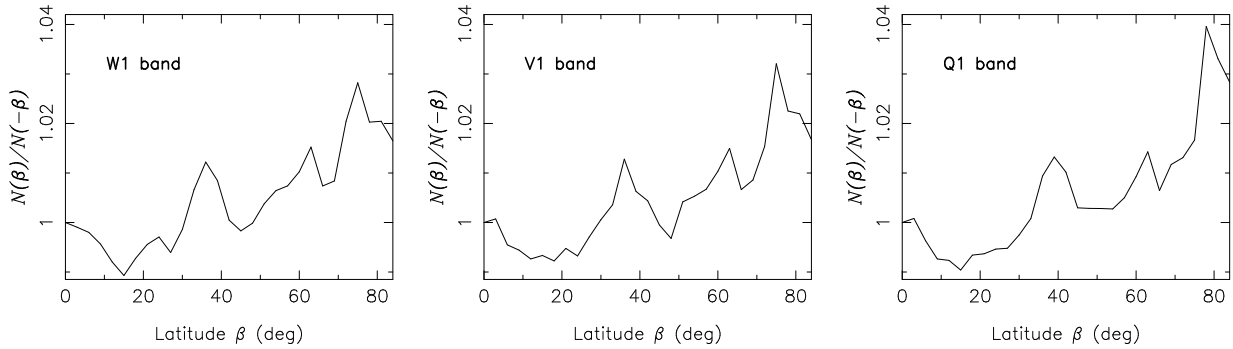


Fig. 9.— North-south asymmetry of WMAP3 exposure.  $N(\beta)$  is the total number of observations contributing to the pixels with ecliptic latitude from  $(\beta - 1.5)$  deg to  $(\beta + 1.5)$  deg in the northern hemisphere,  $N(-\beta)$  is that in the southern hemisphere. *Left panel*, W1 band. *Middle panel*, V1 band. *Right panel*, Q1 band.

### 3. Foreground contamination

Besides the statistical noise, another kind of error in recovered WMAP CMB maps is systematic distortion. From Eq. 5 we can see that in an iteration the temperature estimation at a sky pixel  $i$  is evaluated based on temperatures of many pixels on a circle in the sky sphere  $\theta_{beam}$  (beam separation) apart from the pixel  $i$ , including  $N_i^-$  pixels pointed by minus-horn when plus-horn pointing to  $i$  and  $N_i^+$  pixels pointed by plus-horn when minus-horn pointing to  $i$ . The sky temperature  $t_{k+}$  observed by plus-horn and  $t_{k-}$  by minus-horn are differently placed in the right side of the iterative formula Eq. 5. The iterative solution  $\hat{t}_i$  could be deviated from the true temperature  $t_i$  due to inhomogeneity of temperature sky and unbalance between two sky side beam measurements.

#### 3.1. Map distortion by a hot source

The foreground induced systematic effect on a recovered map is not only limited in the region containing foreground sources, but spreaded over the whole sky. A hot foreground source pointed by the side beam A of a radiometer can distort the recovered temperatures of sky pixels pointed by the side beam B with separation angle  $\theta_{beam}$  to the source through map-making iterations. From Eq. 5 (or Eq. 4) the first iterative solution of temperature of a sky pixel  $i$  can be expressed as

$$t_i^{(1)} = t_i - \langle t - t^{(0)} \rangle_{ring} \quad (8)$$

where  $\langle \rangle_{ring}$  denotes averaging on the scan ring with separation angle  $\theta_{beam}$  to the pixel  $i$ . For zero initials  $t^{(0)} = 0$

$$t_i^{(1)} = t_i - \langle t \rangle_{ring} , \quad (9)$$

a hot source contained on the scan ring will let  $\langle t \rangle_{ring} > 0$  and the recovered temperature  $t_i^{(1)} < 0$ , indicating that a hot foreground source might systematically make the recovered temperatures on its scan ring lower.

A one-dimensional simulation is made to show such effect. A true temperature “sky” containing 500 pixels is produced as a white noise series of zero mean and 0.2 mK standard deviation with a hot source in the pixel interval 240-260, as shown in the upper panel of Fig. 10. To produce differential data, we simulate a scan process of a differential radiometer with instrument noise  $\sigma_0 = 4.0$  mK and beam separation  $\theta_{beam} = 100$  pixel. From  $i = 1$  to 500, for each pixel  $i$  we produce 2500 temperature differences  $t_i - t_j + n$  where  $j = i + 100$  for  $i \leq 400$  or otherwise  $j = i - 400$ ,  $n$  is sampled from the normal distribution with zero mean and standard deviation  $\sigma_0$ . We use Eq. 4 to reconstruct temperature map

from the differential data. For pixel  $k = 350$  the recovered temperatures from first fifteen iterations,  $t_k^{(1)}, t_k^{(2)}, \dots, t_k^{(15)}$  are shown in Fig. 11, where we see that the recovered temperature of first iteration for the pixel  $\theta_{beam}$  away from the hot pixel really drops down dramatically as expected by Eq. 8 and after a few iterations converged to a stable value which still significantly lower than its real temperature. The lower panel of Fig. 10 shows the recovered temperature map after 50 iterations. There exist two significant cold regions in the recovered map with pixels 340 – 360 and 140 – 160, each have a distance of  $\theta_{beam}$  to the hot source interval and their temperature variation negatively related to that of the hot source. Two more regions distorted in the similar way can be found in the recovered map, each placed 100 pixel away from the above two cold regions respectively, pixel intervals 440 – 460 and 40 – 60. The above simulation result indicates that a hot source can distort temperatures in the map recovered from differential data at pixels away from the source with distance of the beam separation and such distortion can propagate to more far away pixels.

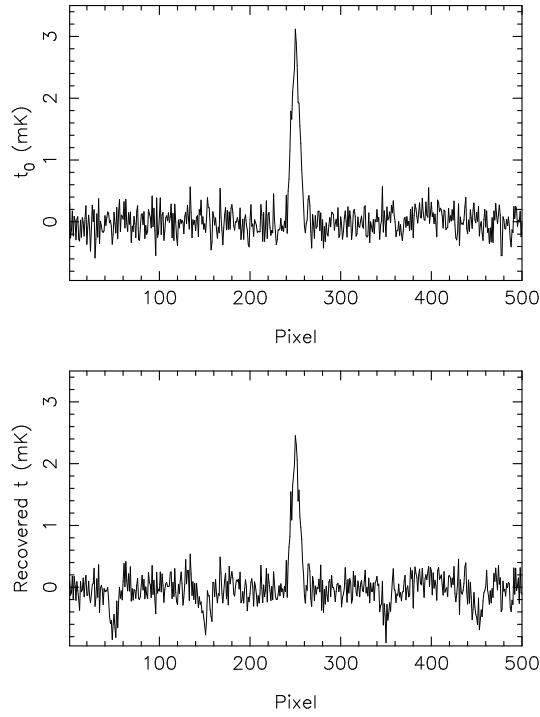


Fig. 10.— True and recovered temperatures. *Upper panel:* True temperatures. *Lower panel:* Recovered temperatures.

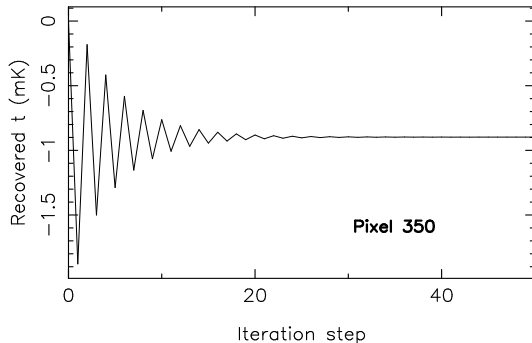


Fig. 11.— Recovered temperature at pixel 350 vs. step number of iteration by map-making Eq. 4. The one-dimensional true temperature map, shown in the upper panel of Fig. 10, has a hot source with a peak at pixel 250, and the differential data is simulated for a radiometer with beam separation of 100 pixel.

### 3.2. 141° rings in WMAP maps

The beam separation angle  $\theta_{beam}$  of WMAP radiometers is 141°. We predict from the above simulation that there should exist strongest negative correlation in WMAP temperature maps between temperatures of two sky pixels separated 141° each other. This prediction is confirmed by analyzing temperature maps in Q, V and W bands released by WMAP team. For the WMAP3 Q-, V- and W-band maps with HEALPix resolution parameter  $N_{side} = 128$  (Gorski et al. 2005), we calculate cross-correlation coefficients  $C_{t_a \langle T_b \rangle}(\theta)$  between  $t_a$  and  $\langle t_b \rangle$  for different separation angle  $\theta$ , where  $t_a$  denotes the temperature of a sky pixel  $a$  and  $\langle t_b \rangle$  the average temperature of the ring with separation angle  $\theta$  to the pixel  $a$ , the obtained distributions are shown in Fig. 12.

From Fig. 12 we find that the strongest negative correlation appear indeed around 141° separation in the correlation distribution for each band. If pixel  $a$  is limited within the sky region of the foreground mask Kp12 (Bennett et al. 2003b) which consists mainly of hot pixels, around 141° separation show more strong negative correlation just as expected from assuming that hot foreground emission induce the correlation.

The program synfast in HEALPix software package (available at <http://healpix.jpl.nasa.gov>) can create temperature maps computed as realizations of random Gaussian fields on a sphere characterized by the user provided spherical harmonic coefficients of a angular power spectrum. To test the significance of the correlation  $C(141^\circ) = -0.238$  in Q-band WMAP map, simulated temperature maps are created with the synfast program from the best fit  $\Lambda$ CDM model power spectrum with Q-band beam function and noise property. For each simulated CMB map, we compute the correlation coefficient between temperatures of the pixels in

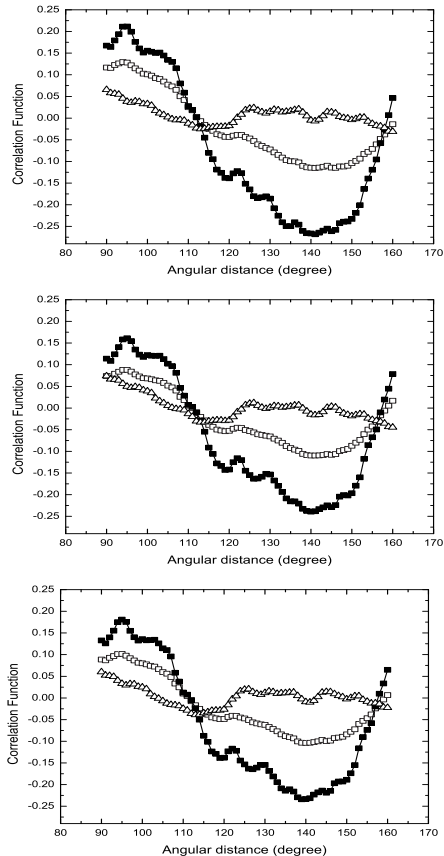


Fig. 12.— Correlation coefficient  $C_{t_a \langle t_b \rangle}(\theta)$  between temperatures  $t_a$  and  $\langle t_b \rangle$  vs. separation angle  $\theta$ .  $t_a$  denotes the temperature of sky pixel  $a$ ,  $\langle t_b \rangle$  the average temperature of the ring with separation angle  $\theta$  to  $a$ . *Filled square*: pixel  $a$  only within the foreground mask Kp12. *Square*: for whole sky. *Triangle*: only for the sky region out of the mask Kp0. *Top panel*: WMAP3 Q-band. *Middle panel*: WMAP3 V-band. *Bottom panel*: WMAP3 W-band.

Kp12 region and average temperatures on their  $141^\circ$  rings. From 1000 simulated maps we get  $C'(141^\circ) = 0.108 \pm 0.080$ , indicating that the  $141^\circ$  negative correlation detected in WMAP Q-band map has a significance of  $4.3\sigma$ . Similarly, for V-band we get  $C(141^\circ) = -0.231$  with significance  $4.4\sigma$  evaluated by  $C'(141^\circ) = 0.099 \pm 0.075$  from simulated CMB maps, and for W-band  $C(141^\circ) = -0.268$  with significance  $5.0\sigma$  from  $C'(141^\circ) = 0.094 \pm 0.072$ .

It is expected from our simulation shown in Fig. 10 that foreground hot sources can produce cold rings of  $141^\circ$  separation in WMAP temperatures. To test this effect, for each sky pixel we calculate the average temperature of its  $141^\circ$  ring from the WMAP3 Q-band, V-band, W-band and ILC temperature maps with  $N_{side} = 128$  and Kp0 mask (Bennett et al. 2003b) for foreground clean. The result is shown in Fig. 13. There is a low

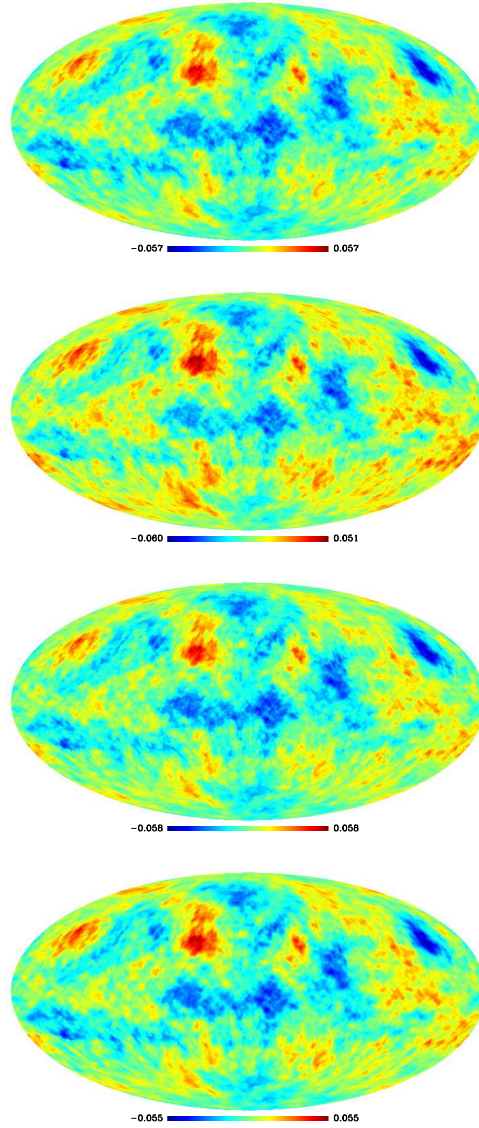


Fig. 13.— Average temperature maps of  $141^\circ$  ring in Galactic coordinates from WMAP3 Q-band, V-band, W-band and ILC map (from top to bottom panel).

temperature region near Galaxy center in Fig. 13 for each band indicating that most of the  $141^\circ$  rings corresponding to the galaxy center region are cold. This is consistent with our expectation.

To roughly estimate the magnitude of temperature distortion by foreground emission, we pick up 2000 hottest pixels in the 3-year WMAP Q-band map and then find out their  $141^\circ$  rings. The average temperature of all pixels on these rings and out of the Kp0 mask (cover about 14% of the sky, see Fig. 14) is calculated to be  $\langle t \rangle = -0.0117$  mK. The correspondent value from 1000 simulated CMB maps is  $\langle t' \rangle = 3.4 \times 10^{-5} \pm 0.006$  mK. Similarly, for V-band we get  $\langle t \rangle = -0.0125$  mK and  $\langle t' \rangle = -4.7 \times 10^{-5} \pm 0.006$  mK, for W-band  $\langle t \rangle = -0.0141$  mK and  $\langle t' \rangle = 8.8 \times 10^{-5} \pm 0.006$  mK. Therefore, in foreground-cleaned WMAP maps, considerable foreground-induced deviations still exist with amplitude comparable to the fluctuation of CMB signal and over broad sky region.

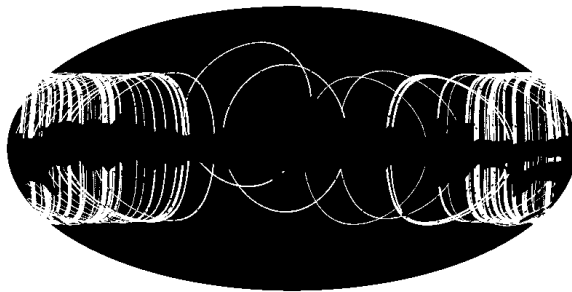


Fig. 14.—  $141^\circ$  rings of 2000 hottest pixels in 3-year Q-band WMAP map, after using the Kp0 mask, in Galactic coordinates.

The foreground-induced deviation in WMAP temperatures should also distort the temperature angular power spectrum. We use simulated temperature maps created with the synfast program to roughly estimate the magnitude of foreground-induced distortion for the WMAP power spectrum on large-scale (low- $l$ ) region. For each simulated map, we subtract 0.01 mK from each temperature of pixels on the  $141^\circ$  rings corresponding to the 2000 hottest pixels (shown in Fig. 14) to get a distorted map. We compute the power spectrum for simulated and distorted map respectively and find that, on average, the deviation between the original and distorted spectrum densities at  $l = 2, 3$  is  $\sim 10\%$ , indicating that the foreground-induced distortion on WMAP power spectrum cannot be ignored for a precision cosmology study. Strongest hot sources may produce cold spots by the foreground induced distortion out of the foreground region. Temperature distortions in a CMB map caused by foreground sources with different scales and observation dependent noise could distort the

angular power spectrum on wide range of angular scale.

### 3.3. Large non-Gaussian spots

A large cold spots with a radius of  $\sim 5^\circ$  centered at  $(l, b) = (209^\circ, -57^\circ)$  and the lowest temperature  $\sim -0.15$  mK has been detected in WMAP1 and WMAP3 maps with the wavelet and other techniques (Vielva et al. 2004; Cruz et al. 2005; Cruz et al. 2006; Cruz et al. 2007a; Vielva et al. 2007), and was explained as a cosmic texture, a remnant of symmetry-breaking at energies close to the Planck scale in the very early universe (Cruz et al. 2007b). We find that the  $141^\circ$  rings of the pixels in the spot region across through the hot Galactic plane with temperature up to  $\sim 5$  mK, therefore, the foreground induced systematic effect on recovered maps discussed in §3.1 should be a more plausible explanation to the detected large cold spot than the texture hypothesis. The foreground contamination and other systematic effect may also produce other more detected large spots in WMAP maps.

## 4. Discussion

### 4.1. Can the exposure induced anisotropy be corrected ?

It has to be pointed out that Eq. 7 can be used to modify the effect of exposure dependent noise, like what we do for the latitude distribution of rms variation shown in Fig. 2, only for the case that the map rms fluctuation  $\langle t^2 \rangle$  itself is the directly analyzed quantity. However, almost all analysis works are based on CMB maps of temperature. We know from Figs. 2-5 that the released WMAP temperature maps contain considerable exposure dependent noise. It is no way from a recovered temperature map to produce a corrected map in which the instrument-induced and exposure-dependent noise can be eliminated. Therefore, the anisotropy noise should contribute to large scale anomalies detected in existent CMB maps.

The exposure inhomogeneity of WMAP comes from its scan strategy, which can't be suppressed through accumulating observation time. To avoid the observation effect, it is needed to remake temperature maps from a uniform differential data set obtained by giving up partial observation data for pixels of high exposure. Comparing released WMAP maps and new maps from uniform data will help us to judge their origin of detected large scale anomalies, e.g. the low  $l$  power issues detected in WMAP data, the unexplained orientation of large-scale patterns of CMB maps in respect to the ecliptic frame, the north-south asymmetry of temperature fluctuation power etc., and to see if the observational effect can also influence the angular power spectrum as well.

## 4.2. Avoiding the foreground-induced distortion

The distortion by hot foreground sources on their  $141^\circ$  rings in a WMAP map can not be removed with a foreground mask on the recovered temperature map. What's needed is to use the mask on the original differential data before map-making to avoid the foreground-induced error in the recovered map. The top panel of Fig. 15 shows the difference between the recovered and true temperature distributions (shown in the lower and upper panel of Fig. 10 respectively), where the distortion structure caused by the hot source on pixel 240 - 260 and beam separation of 100 pixel is clearly shown. We redo the temperature reconstruction with excluding the temperature differences that contain a beam side pointing to a pixel between 240 - 260 (“mask region”) during iterations for the pixels out of mask, the result is shown in the middle panel of Fig. 14, where the distortion structures are really suppressed.

A weakness of using mask in map-making process is decreasing the number of useful differential data. Another approach to avoid the distortion in recovered map by foreground emission is to properly set the initials of iteration for the foreground region. From Eq. 8 we see that the temperature deviation of the first iterative solution,  $t_i^{(1)} - t_i$ , will be suppressed if the temperature initials at pixels of hot source are set to be close to their true values to let  $\langle t - t^{(0)} \rangle_{ring} \approx 0$ . The initial  $t_i^{(0)}$  of pixel  $i$  can be taken as

$$t_i^{(0)} = \frac{1}{N'_i} \left( \sum_{k^+=i} d_k - \sum_{k^-=i} d_k \right). \quad (10)$$

Where  $\sum_{k^+=i}$  means summing over the observations while the pixel  $i$  is observed by the plus-horn and the pixel pointed by the minus-horn is out of mask,  $\sum_{k^-=i}$  means summing over the observations while the pixel  $i$  is observed by the minus-horn and the pixel pointed by the plus-horn is out of mask,  $N'_i$  is the total number of used observations. For the simulated differential data from the true temperatures shown in the upper panel of Fig. 10, we make 50 iterations with Eq. 4 starting from initials calculated by Eq. 10, the distortion structures are satisfactory suppressed in the resultant solution, as shown in the bottom panel of Fig. 15.

## 4.3. Remaking WMAP maps

We demonstrate in this paper that for existent CMB maps both the observation dependent noise and systematic error induced by foreground emission can not be neglected and both can produce large-scale anomalies and distort the angular power spectrum. These errors can not be completely excluded by performing noise suppressing or using foreground mask on temperature maps. We suggest to remake temperature maps from the original WMAP time-order-data by a modified algorithm with applying foreground mask in map-making to

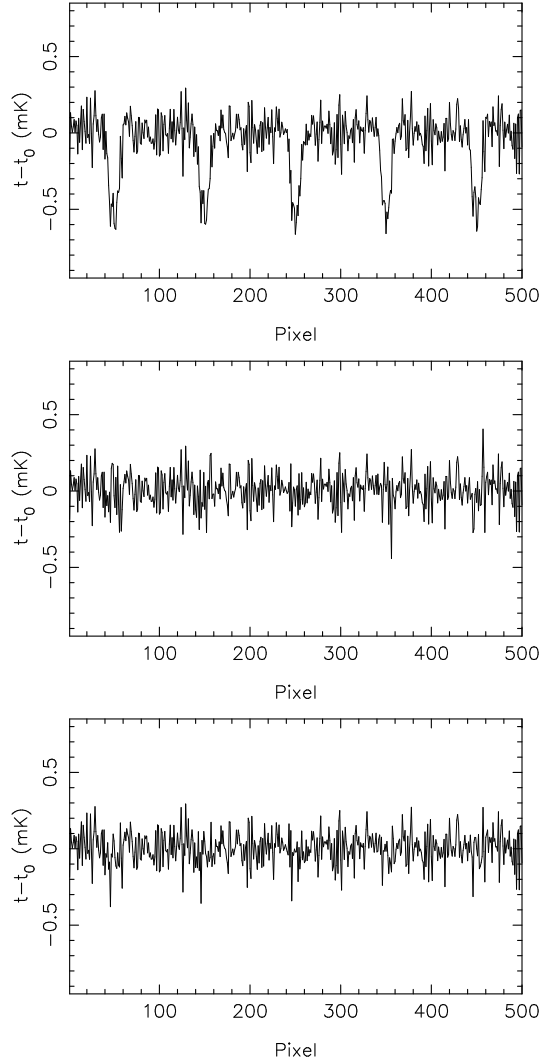


Fig. 15.— Differences between recovered  $t$  and true temperature  $t_0$ . The one-dimensional temperature distribution  $t_0$  consists of white noise and hot source between 240 - 260 pixel (mask region), as shown in the upper panel of Fig. 10. Differential data is obtained by simulation of one-dimensional scan for  $t_0$  by a differential radiometer with beam-separation of 100 pixel. Recovered  $t$  are calculated with map-making Eq. 4 after 50 iterations. *Upper panel:*  $t$  recovered from all differential data (the lower panel of Fig. 10). *Middle panel:*  $t$  recovered by iterations from all data for mask region and with excluding differences that contain hot source temperature for pixels out of mask. *Bottom panel:*  $t$  recovered by iterations with initials estimated from the differential data by Eq. 10.

exclude mask pixels from use in iterations for CMB dominated region (or properly set temperature initials before iteration), and/or keeping used differential data uniform by giving up partial observation data for pixels of high exposure. New maps from modified map-making algorithm will help us to judge the origin of large scale anomalies detected in released WMAP maps, e.g. the low  $l$  power issues, the unexplained orientation of large-scale patterns in respect to the ecliptic frame, the north-south asymmetry of temperature fluctuation power and the large non-Gaussian spots, and to see to what extent the statistical and systematical errors influence the angular power spectrum and the derived cosmological parameters. Believable conclusions on CMB anisotropy anomalies and precise temperature angular power spectrum from differential measurement should be based on temperature maps with homogeneous sky exposure and should avoid foreground-induced distortion during map-making.

This study is supported by the National Natural Science Foundation of China and the CAS project KJCX2-YW-T03. The data analysis in this work made use of the WMAP data archive and the HEALPIX software package.

## REFERENCES

- Abramo L.R., Bernui A., Ferreira I.S., Villela T. & Wuensche C.A., 2006, *Phys. Rev. D*, 74, 063560
- Bennett, C.L. et al., 2003c, *ApJ*, 583, 1
- Bennett, C.L. et al., 2003b, *ApJS*, 148, 1
- Bennett, C.L. et al., 2003c, *ApJS*, 148, 97
- Copi, C.J., Huterer, D., Schwarz, D.J. & Starkman, G.D., 2006, *MNRAS*, 367, 79
- Copi, C.J., Huterer, D., Schwarz, D.J. & Starkman, G.D., 2007, *Phys. Rev. D*, 75, 023507
- Cruz M., Martinez-Gonzalez E., Vielva P. & Cayon L., 2005, *MNRAS*, 356, 29
- Cruz M., Tucci M., Martinez-Gonzalez E. & Vielva P., 2006, *MNRAS*, 369, 57
- Cruz M., Cayon L., Martinez-Gonzalez E. & Vielva P., 2007a, *ApJ*, 655, 11
- Cruz, M., Turok, N., Vielva, P., Martinez-Gonzalez E. & Hobson M., *Science*, 2007b, 318, 1612
- de Oliveira-Costa, A., Tegmark, M., Zaldarriaga. & Hamilton A., 2004, *Phys. Rev. D*, 69, 063516

- Eriksen H.K., Hansen, F.K, Banday, A.J., Grski, K.M. & Lilje, P.B., 2004a, ApJ, 605, 14
- Eriksen H.K., Banday A.J., Gorski K.M. & Lilje, P.B., 2004b, ApJ, 612, 633
- Eriksen H.K., Banday, A.J., Grski, K.M. Hansen, F.K & Lilje, P.B., 2007, ApJ, 660, L81
- Gorski, K. M., Hivon, E., Banday, A. J., Wandelt, B. D., Hansen, F. K., Reinecke, M., Bartelmann, M., 2005, ApJ, 622, 759
- Hansen F.K., Banday A.J. & Gorski K.M., 2004, MNRAS, 354, 641
- Hinshaw, G. et al., 2003, ApJS, 148, 63
- Hinshaw, G. et al., 2007, ApJS, 170, 288
- Jaffe T.R., Banday A.J., Eriksen H.K.,Gorski K.M. & Hansen F.K., 2005, ApJ, 629, L1
- Jaffe T.R., Banday A.J., Eriksen H.K.,Gorski K.M. & Hansen F.K., 2006, A&A, 460, 393
- Land K. & Magueijo J., 2007, MNRAS, 378, 153
- Li T.P. & Wolfendale A.W., 1982, A&A, 116, 95
- Limon, M. et al., 2003, *Wilkinson Microwave Anisotropy Probe (WMAP) : Explanatory Supplement*, Greenbelt, MD: NASA/GSFC; Available in electronic form at <http://lambda.gsfc.nasa.gov/>
- Park C.G., Park C. & Gott J.R., 2007, ApJ, 660, 959
- Samal, P.K., Saha, R., Jian, P. & Ralston, J.P., 2008, MNRAS, 385, 1718
- Schwarz, D.J., Starkman, G.D., Huterer, D. & Copi, C.J., 2004, Phys. Rev. Lett., 93, 221301
- Spergel D. N. et al., 2006, arXiv:astro-ph/0603449v1
- Starkman, G.D. & Schwarz, D.J., 2005, Sci. Am., 293(2), 48
- Smoot, G.F. et al., 1990, ApJ, 360, 685
- Smoot, G.F. et al., 1991, ApJ, 371, L1
- Tegmark, M., de Oliveira-Costa, A. & Hamilton, A.J., 2003, Phys. Rev. D, 68, 123523
- Vielva P., Martinez-Gonzalez E., Barreiro R. B., Sanz J. L., Cayon L., 2004, ApJ, 609, 22
- Vielva P., Wiaux Y., Martinez-Gonzalez E. & Vandergheynst P., 2007, MNRAS, 381, 932

